communications earth & environment

ARTICLE

https://doi.org/10.1038/s43247-022-00368-y OPEN

# The unexpectedly short Holocene Humid Period in Northern Arabia

Ina Neugebauer[1,2], Michèle Dinies[3,4], Birgit Plessen[1], Nadine Dräger[1], Achim Brauer[1], Helmut Brückner[5], Peter Frenzel[6], Gerd Gleixner[7], Philipp Hoelzmann[4], Kim J. Krahn[8], Anna Pint[6], Valérie F. Schwab[7], Anja Schwarz[8], Rik Tjallingii[1] & Max Engel[9,10]✉

The early to middle Holocene Humid Period led to a greening of today's arid Saharo-Arabian desert belt. While this phase is well defined in North Africa and the Southern Arabian Peninsula, robust evidence from Northern Arabia is lacking. Here we fill this gap with unprecedented annually to sub-decadally resolved proxy data from Tayma, the only known varved lake sediments in Northern Arabia. Based on stable isotopes, micro-facies analyses and varve and radiocarbon dating, we distinguish five phases of lake development and show that the wet phase in Northern Arabia from 8800–7900 years BP is considerably shorter than the commonly defined Holocene Humid Period (~11,000–5500 years BP). Moreover, we find a two century-long peak humidity at times when a centennial-scale dry anomaly around 8200 years BP interrupted the Holocene Humid Period in adjacent regions. The short humid phase possibly favoured Neolithic migrations into Northern Arabia representing a strong human response to environmental changes.

[1] GFZ German Research Centre for Geosciences, Section Climate Dynamics and Landscape Evolution, Telegrafenberg, 14473 Potsdam, Germany. [2] University of Geneva, Department of Earth Sciences, Rue des Maraichers 13, 1205 Genève, Switzerland. [3] German Archaeological Institute (DAI), Scientific Department of the Head Office, Im Dol 2–6, 14195 Berlin, Germany. [4] Freie Universität Berlin, Institute of Geographical Sciences, Malteser Str. 74-100, 12249 Berlin, Germany. [5] University of Cologne, Institute of Geography, Zülpicher Str. 45, 50674 Köln, Germany. [6] Friedrich Schiller University Jena, Institute of Earth Sciences, Burgweg 11, 07749 Jena, Germany. [7] Max Planck Institute for Biogeochemistry, Research Group Molecular Biogeochemistry, Hans-Knöll-Str. 10, 07745 Jena, Germany. [8] Technische Universität Braunschweig, Institute of Geosystems and Bioindication, Langer Kamp 19c, 38106 Braunschweig, Germany. [9] Heidelberg University, Institute of Geography, Im Neuenheimer Feld 348, 69120 Heidelberg, Germany. [10] Royal Belgian Institute of Natural Sciences, Geological Survey of Belgium, Jennerstraat 13, 1000 Brussels, Belgium. ✉email: max.engel@uni-heidelberg.de

Past millennial-scale pluvial periods driven by precession-forced intensification of summer monsoons and northward migration of associated rainfall are thought to have facilitated human dispersal out of Africa[1–3] by providing 'green corridors' through today's arid Saharo-Arabian desert belt[4–6]. Research on human–climate interaction on the Arabian Peninsula has intensified only recently, even though the region demonstrates high ecological sensitivity to climatic changes and represents the geographic nexus between Africa and Asia[1–3,7,8]. This recent wave of research in Arabia has already fundamentally transformed our perception of Arabian prehistory, including discoveries of Middle Palaeolithic (MIS 5 or even older) sites in Central Arabia[9] or traces of *Homo sapiens* in the Nefud desert at approximately 87 ka[8], i.e. phases associated with conditions more humid than today[2,6]. One of the emerging topics is the role of the early to middle Holocene Humid Period (HHP) in Neolithic migrations and cultural progress[10,11].

Climate models suggest that the African Summer Monsoon (ASM) was the dominant moisture source on the Arabian Peninsula during pluvials[1,12]. Yet, this remains a matter of debate for the Northern Arabian desert[13–15], as stronger insolation intensified and extended both ASM[1,2,12,16–18] and, possibly, Mediterranean winter rains[3,19]. The latter system is the main source of moisture in this region today. In addition, tropical plumes (TPs), i.e. synoptic disturbances conveying water vapour as continuous mid-upper tropospheric cloud bands from the Intertropical Convergence Zone (ITCZ) to >15°N, are known to affect Northern Arabia during winter and spring[14,20,21]. Higher frequency of such patterns during past pluvials was suggested to have contributed increased rainfall to the Saharo-Arabian desert[14,22,23], even though their past role as a moisture source remains poorly understood.

The rich archaeological heritage of Arabia is currently being investigated by major research initiatives[7,11,24]. "Potentially thousands of water bodies" have been reconstructed for past pluvials[25], but it is still unknown how these water bodies and human habitats exactly looked like and for how long they existed[14,15]. Only a few climate records are available from speleothems in the wider region, i.e. the Levant[26–28] and Southern Arabia[29,30]. The entire lack of high-resolution palaeoclimate data from Northern Arabia leads to an inconsistent picture about the timing and magnitude of the HHP for this culturally important corridor to the Middle East, where some lower-resolution lacustrine records have pointed to more humid conditions during the last interglacial (MIS 5) and the early to mid-Holocene[10,17,31–33].

The Tayma palaeolake record[4,34] is the only known high-resolution archive of the HHP in Northern Arabia providing insights into the early to mid-Holocene hydroclimate variability in unprecedented detail. The 20 $km^2$-sized inland sabkha of Tayma has a 660 $km^2$ hydrological catchment (Fig. 1; Supplementary Figs. 1 and 2) and is located at 27°40′N within the arid desert's interior. It receives only scarce rains (on average 45 mm $a^{-1}$) from Mediterranean winter storms, occasional cross-Saharan TPs or the Red Sea cyclones between autumn and spring[14] (Fig. 1). Previous investigations of shoreline deposits (Supplementary Figs. 3–5) and sediment cores from the sabkha basin indicate the existence of a >17 m deep, perennial groundwater-supported lake[15] and the spread of grassland[4] during the early Holocene. The catchment-lake ratio (Fig. 1b; Supplementary Fig. 1b) and the short duration of this peak lake phase[4,15,34] exclude the influence of tectonics on lake-level changes, emphasising the significance of the lake as a palaeoclimate archive that is mainly controlled by rainfall, groundwater inflow and evaporation (see also Supplementary Note 1 for details on controlling processes of the sedimentary archive). Yet, a precise determination of the timing of the lake phases was still missing, preventing a detailed view of the evolution of the palaeolake and the palaeoclimatological implications.

In this paper, we decipher five phases of lake development at Tayma and show that the HHP in Northern Arabia from 8800 to 7900 years BP is shorter than commonly defined (~11,000–5500 years BP). Interestingly, we identify a two century-long peak humidity at Tayma overlapping with a centennial-scale dry anomaly around 8200 years BP that interrupted the HHP in adjacent regions. The results clearly demonstrate that regional patterns in palaeoclimate were more complex and spatially small-scale than previously assumed.

## Results

**Chronology of the Tayma palaeolake record**. The Tayma palaeolake record partly contains annually laminated sediments that were counted under the microscope (see Methods, Fig. 2, Supplementary Fig. 9). The new high-resolution age-depth model integrates AMS radiocarbon ages of pollen concentrates, microscopic varve counting and the independent age of a cryptotephra[35] in a Bayesian model (see Methods, Supplementary Data 1, Supplementary Fig. 7). The floating varve chronology comprising 650 ± 40 couplets is anchored to the radiocarbon age scale and constrains the varved lake phase at Tayma to 8550–7900 ± 40 cal varve yr BP (±90 cal yr BP including the $^{14}C$ calibration error). A robust time marker is provided by the identification of the central Anatolian 'S1' tephra in the lower part of the record, dated to 8983 ± 83 cal yr BP in the Dead Sea record[34]. The lacustrine and wetland sediments in the Tayma basin were deposited from ca. 9250 to ca. 4200 cal yr BP (Supplementary Fig. 7).

**Changes in precipitation and evaporation signals in the Tayma record**. Compound-specific hydrogen isotope compositions of plant-wax n-alkanes ($\delta D_{nC29,\ nC31}$), as well as porewater, rainwater and groundwater isotopes ($\delta^{18}O_{water}$ and $\delta D_{water}$) trace variations in moisture supply and rainfall amount (Fig. 2, Methods and Supplementary Fig. 8). Stable oxygen and carbon isotope compositions of single primary aragonite laminae from the varved core section ($\delta^{18}O_{arag}$ and $\delta^{13}C_{arag}$) and of bulk carbonates from the entire core ($\delta^{18}O_{carb}$ and $\delta^{13}C_{carb}$) indicate changing groundwater and surface-water inflow, lake-water evaporation and lake-internal productivity (Fig. 2). The most striking finding was terrestrial plant wax $\delta D_{nC29,\ nC31}$ values of about −100‰ during the shallow lake or wetland phase and much lighter values down to −150‰ during the palaeolake phase. These data reflect higher rainfall between 8800 and 7950 cal yr BP due to increased precipitation and a probable amount effect (Methods and Supplementary Fig. 8).

**Evolution of the Tayma palaeolake**. The evolution of the lake can be separated into phases I–V, followed by phases VI (wetland) and VII (sabkha). A basal zone of brownish-grey carbonate mud with irregular, coarse carbonate lamination from 9250 to 8800 cal yr BP (lake phase I) (Supplementary Fig. 6) represents a shallow lake initiated by increasing rainfall and recharge of the local Saq aquifer when clastic sediments were deposited in a deflated endorheic basin from a prevailing desert environment[4]. Carbonates precipitated with very high $\delta^{18}O_{carb}$ values of around +11‰ and low $\delta^{13}C_{carb}$ values of around -8‰.

At ca. 8800 cal yr BP (lake phase II), a sharp decrease of $\delta^{18}O_{carb}$ to +8‰, increasing $\delta^{13}C_{carb}$ (Fig. 2) and the in situ deposition of the brackish-water ostracod *Cyprideis torosa* (Fig. 2e) indicate reduced lake-water evaporation and the initial establishment of a shallow, but perennial and increasingly productive water body[36] as a response to wetter conditions.

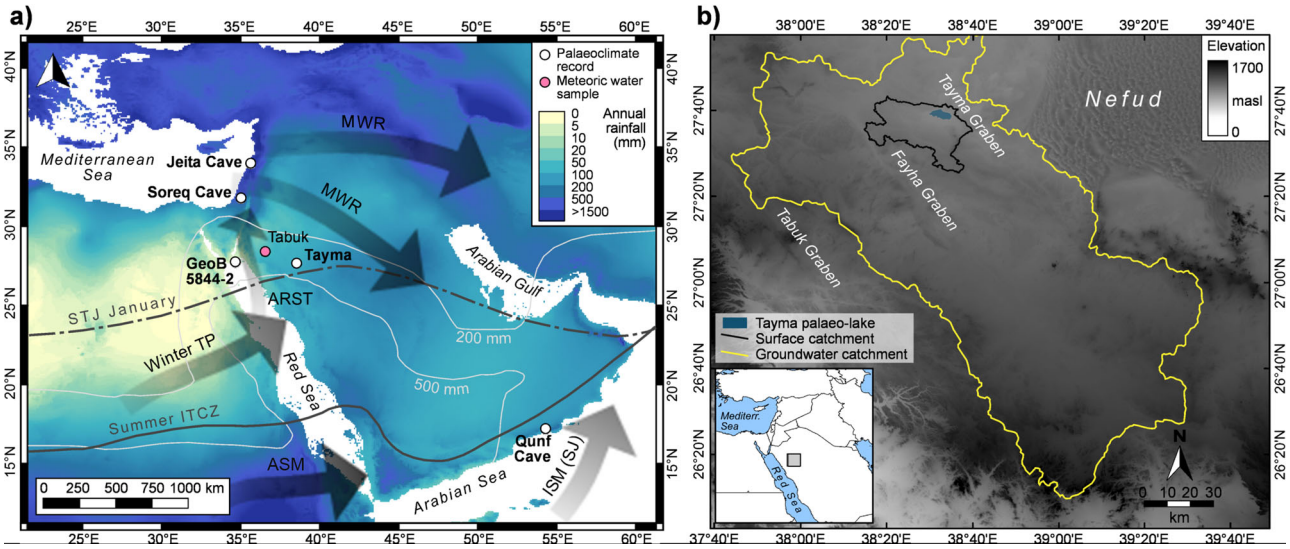


**Fig. 1 Regional setting of Tayma. a** Overview of the Arabian Peninsula and adjacent areas with the key palaeoclimate sites of Jeita Cave[28], Soreq Cave[26,27], GeoB 5844-2 in the Red Sea[13] and Qunf Cave[29], mean annual rainfall 1970–2000 (WorldClim 2 dataset[77]), average positions of the Intertropical Convergence Zone (ITCZ) in summer and the Subtropical Jet (STJ) in winter[78], and atmospheric sources of regional precipitation (MWR Mediterranean winter rains, Winter TP winter tropical plumes, ASM African Summer Monsoon, ISM (SJ) Indian Summer Monsoon (Somali Jet), ARST Active Red Sea Trough)[14]. Isohyetes of 200 mm and 500 mm are adapted from the wettest simulation of the COSMOS climate model at 6000 BCE in ref. [12]. **b** Reconstructed extent of the Tayma palaeolake during its peak phase, today's surface catchment and groundwater catchment[79]. The topography is based on GTOPO30 data[80].

The $\delta D_{nC29,\ C31}$ values show a strong variability between −140‰ and −90‰.

At ca. 8550 cal yr BP the formation of varves started (Fig. 2; Supplementary Figs. 6 and 9). Fine lamination over a period of 650 ± 40 varve years (lake phases III and IV) reflects the onset of a deep (>17 m[15], Supplementary Figs. 3–5) and stratified permanent lake, similar and coeval to, e.g. the Awafi palaeolake at Ras Al-Khaimah, United Arab Emirates[37]. From ca. 8550 to 8250 cal yr BP (lake phase III), variable but continuously decreasing plant wax $\delta D_{nC29,\ nC31}$ values between −150 and −100‰ indicate a humid period with enhanced seasonality[38,39]. The alternating deposition of dark clastic, clay- and organic-rich laminae and white, primary aragonite laminae reflects pronounced wet and dry seasons. Suspension grading observed in some of the clastic varves indicates wadi activation and fluvial sediment input into a standing water body during the wet season. The aragonite laminae represent the arid season of enhanced evaporation, reduced or absent surface-water input, lake contraction and lake-level fall, as well as increased concentration of soluble matter[40]. The highest concentrations of brine occur near the water surface, where aragonite crystals form and settle through the water column as pelagic rain[41,42]. The $\delta^{18}O_{carb}$ values generally decrease from +8‰ to +6‰ simultaneously with progressively increasing $\delta^{13}C_{carb}$ values from about −6 up to +2‰ toward enhanced lake productivity[43,44]. The positive excursion of $\delta^{18}O_{carb}$ to >+10‰ centred at ca. 8400 cal yr BP reflects a decadal- to centennial-scale drawback to even stronger dry-season evaporation. This intensified dry-season evaporation was compensated by enhanced humidity during the rainy season and groundwater inflow, indicated by the decreasing trend of $\delta D_{nC29,\ nC31}$ at that time, data which mostly reflects the wet season of leaf growth[39]. This rainy-season moisture surplus was sufficient to sustain a high lake level and varve formation.

The phase between ca. 8250 and 7950 cal yr BP (lake phase IV) shows the highest production rate of organic matter in the lake and annual blooms of planktonic diatoms (mainly *Cyclotella* cf. *choctawhatcheeana*) (Supplementary Figs. 6 and 9). In combination with the greatest abundances of foraminifera, the lowest $\delta D_{nC29,\ nC31}$ values down to −155‰ and weakest dry-season evaporation with lowest $\delta^{18}O_{carb}$ values of +4‰, they indicate the highest lake stand and most humid period at Tayma during the Holocene. This is supported by a distinct change in varve composition from evaporation-driven aragonite varves to pronounced productivity-driven diatom-aragonite varves and total organic carbon (TOC) contents of up to 5%. The highest ratio between $\delta^{13}C_{carb}$ and $\delta^{18}O_{carb}$ in this part of the core is related to phytoplankton bloom controlled by $^{12}C$ depletion due to photosynthetic uptake of $CO_2$, and higher precipitation–evaporation balance[43]. From about 8200 cal yr BP the $\delta D_{nC29,\ nC31}$ values again start to vary between −140‰ and −100‰, and the $\delta^{18}O_{carb}$ values increase from +4 to +8‰ (Fig. 2; Supplementary Fig. 6).

At ca. 7950 cal yr BP, ceasing diatom and aragonite laminae and more abundant clastic quartz grains of aeolian origin, as well as the first appearance of gypsum (Supplementary Figs. 6 and 9), show a rapidly declining lake level (lake phase V). The increased mobility of sand grains indicates a regional decline of vegetation cover, the retreat of grasslands and the establishment of drought-resistant steppe vegetation[4]. The occurrence of gypsum is related to the enrichment of $Ca^{2+}$ ions in the contracting water body and sulphate dissolved in the reduced groundwater and surface water inflow[45]. This led to the disappearance of varves within a few decades, accompanied by a sharp reduction in TOC content and a decline of $\delta^{13}C_{carb}$ back to a level comparable to the early shallow-lake phase II, prior to 8550 cal yr BP. Progressively enriched $\delta D_{nC29,\ nC31}$ values of up to −60‰ and $\delta^{18}O_{carb}$ values toward +12‰ reflect the decrease in surface-water and groundwater inflow and a strongly increasing evaporation, indicating a gradual end of the humid phase over 100–150 years until ca. 7800 cal yr BP.

Further increasing gypsum and Mg–carbonate precipitation and $\delta^{18}O_{carb}$ rising to +12‰ (Fig. 2; Supplementary Fig. 6) point to a shrinking lake and concentration of brine under an increasingly arid climate between 7800 and ca. 6800 cal yr BP.

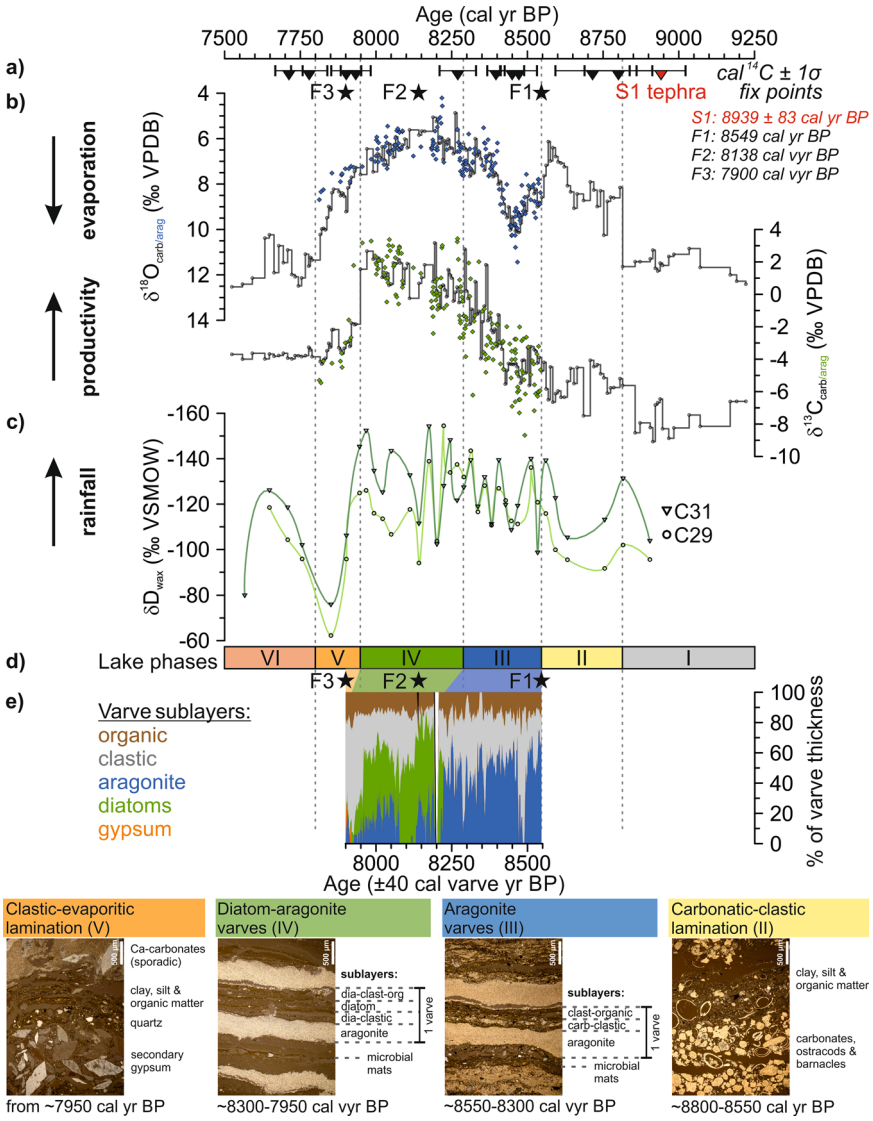


**Fig. 2 Palaeolake evolution in Tayma between 9250 and 7500 cal yr BP. a** Radiocarbon ages (triangles) and fix points (stars; see Methods); **b** $\delta^{18}O_{carb/arag}$ and $\delta^{13}C_{carb/arag}$ measured on bulk carbonates (solid lines) and on single aragonite layers (blue and green diamonds); **c** $\delta D_{wax}$ of *n*-alkanes $nC_{31}$ and $nC_{29}$ ($\delta D_{nC29,\ nC31}$); **d** Tayma lake phases I–V and wetland phase VI; **e** varve sublayers expressed as % of varve thickness for the varve chronology 8550–7900 ± 40 cal varve yr BP, and microscope photographs of thin sections highlighting different micro-facies of lake phases II–V.

At that time, wetland conditions set in with TOC levels close to 0 and further increasing aeolian influx (phase VI). Around ca. 4200 cal yr BP, greyish mud is replaced by reddish-brown, oxidised, mainly aeolian clastics mixed with gypsum (phase VII) (Supplementary Figs. 6 and 7). This pattern reflects temporary desiccation and a further aridification pulse correlating with a dry event recorded at several sites in the Eastern Mediterranean/Middle East, e.g. the Northern Red Sea[46].

## Discussion

Our data support existing low-resolution Northern Arabian palaeoenvironmental records[10,11,31], but they also show that the HHP in Northern Arabia was remarkably short, its peak lasting only ca. 650 years from 8550 to 7900 cal yr BP. A temporary intensification and northeastward shift of the ASM to provide increased rainfall in northwestern Arabia around Tayma during the short HHP is supported by the $\delta^{18}O_{water}$ and $\delta D_{water}$ data. The evaporation line calculated from modern water samples around Tayma and the palaeolake data best fits the isotope data from δD-depleted ASM precipitation at Khartoum, Sudan[47] (Supplementary Fig. 8). The ASM fuelling the HHP in Northern Arabia has also been suggested by several proxy-based[17,32] and climate modelling[1,12,16] studies. We propose a moderate influence of the ASM during the HHP, as Tayma is located at the fringes of the ASM influence at that time[12].

In addition, we observe an intriguing regional hydroclimatic diversity, since the aforementioned peak humidity in Northern Arabia from 8550 to 7900 cal yr BP coincides with a widespread, centennial-scale dry and cool anomaly centred around the 8.2 ka cold event at other low-latitude sites in the Northern Hemisphere such as the Eastern Mediterranean or Southern Arabia[48] (Fig. 3). A low-latitude dry period between ca. 8500 and 7800 cal yr BP was the most pronounced hydroclimatic drawback of the HHP (Fig. 3a). It is evidenced, e.g. in the desiccation or temporary lowstands of North African lakes[49] (Fig. 3f), slightly heavier $\delta^{18}O$ values in Northern Red Sea planktonic foraminifera[13] (Fig. 3e) and diminished runoff of the Nile River[50], leading to re-oxygenation of the Eastern Mediterranean Sea and interruption of sapropel S1[51,52] (Fig. 3b). Drier conditions mostly resulted

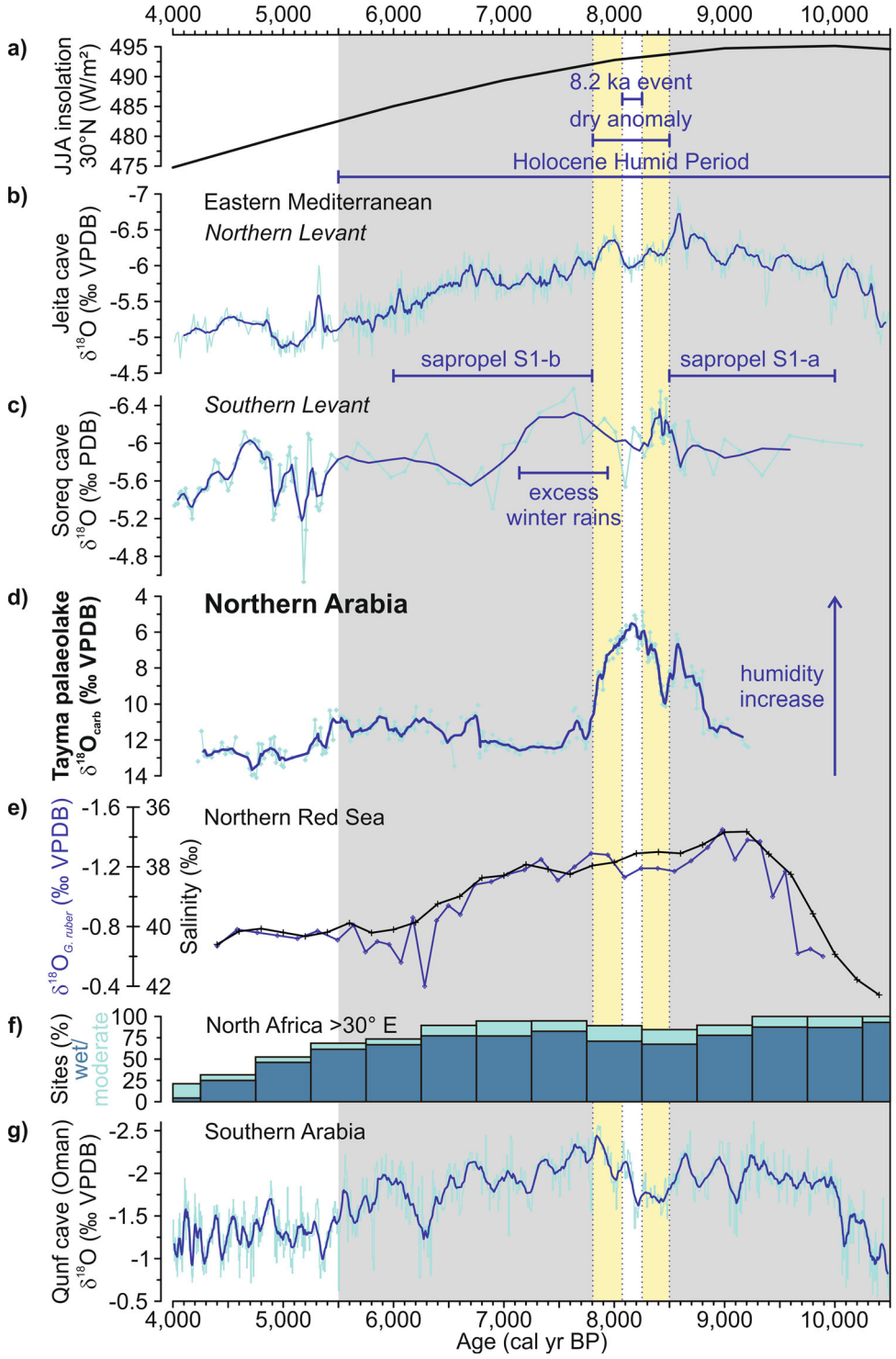


**Fig. 3 Oxygen isotopes recording humidity changes during the early to middle Holocene Humid Period (HHP) across the Eastern Mediterranean to Southern Arabia regions. a** Summer insolation at 30°N[81], duration of the HHP *sensu* ref. [18] (grey), the low-latitude dry anomaly[48] (yellow), and the 8.2 ka cold event in Greenland ice cores[82] (white bar); **b** speleothem $\delta^{18}O$ from Jeita cave (Lebanon)[28], and **c** Soreq cave (Israel)[26,27], with the timing of sapropel formation in the Eastern Mediterranean Sea and excess winter rain in the Southern Levant[51]; **d** $\delta^{18}O_{carb}$ from the Tayma palaeolake (this study); **e** $\delta^{18}O_{G.\ ruber}$ reflecting temperature, and calculated salinity changes from the Northern Red Sea (GeoB 5844-2)[13]; **f** frequency histograms of lake records reflecting wet or moderately wet conditions in the East African Summer Monsoon domain >30°E[18]; **g** speleothem $\delta^{18}O$ from Qunf cave (Oman)[29]. All $\delta^{18}O$ scales are reversed to reflect higher humidity upwards. Palaeoclimate sites are shown in Fig. 1a.

from reduced summer–monsoon rainfall[29,30]. However, speleothem records from the Levantine region[26] (Jeita and Soreq caves; Fig. 3b, c) and marine records from the Eastern Mediterranean suggest that Mediterranean winter rains might have been reduced as well, as a result of temporary, meltwater-related deceleration of the North Atlantic thermohaline circulation[48,53] (Fig. 3). The inference of moderately higher than average rainfall during the HHP from the Soreq speleothem record, mostly during the phase of excess winter rains between 8000 and 7000 cal yr BP, is based on the recalculation of the $\delta^{18}O$ data in ref. [51] eliminating the source effect, i.e. the bias through changes of isotopic composition in the Eastern Mediterranean surface waters[28].

These smaller-scale, regional discrepancies may be explained by the additional contribution of synoptic-scale patterns, which are scarce today. They may have played a more dominant role in delivering moisture to Northern Arabia between 8250 and 8000 cal yr BP resulting in a humidity peak at Tayma. In particular, more frequent TPs may have led to a regional moisture surplus in Northern Arabia. In contrast to short and localised convective cells of the Active Red Sea Trough pattern triggering flash floods in the Southern Levant, TPs promote long-lasting moderate rains and thus more effective moisture over a slightly larger region[20]. TP formation was likely favoured by ocean-atmosphere feedbacks during the 'cool poles—dry tropics' anomaly around 8.2 ka: lower sea-surface temperatures in the North Atlantic and the Mediterranean Sea promote deeper, southwards penetrating mid-latitude troughs and stronger sub-tropical anticyclones (i.e. drier air masses). This leads to an intensification of tropical moisture advection and the sub-tropical jet stream, inducing jet streaks that reach as far as northern tropical West Africa and convey moist air to Northern Arabia at mid-to-upper tropospheric levels[21]. The regionally and chronologically confined enhanced contribution of TPs may have compensated the weakened ASM around 8.2 ka and contributed to the strong seasonal pattern reflected by high-level, high-amplitude $\delta^{18}O_{carb}$ and $\delta D_{nC29,\ nC31}$ data. Mediterranean westerlies as a source of additional winter rainfall, however, seem unlikely, as climate models indicate an even lower intensity during the HHP compared to today[12].

There is multiple evidence that the observed moisture surplus of 8550–7900 cal yr BP identified in the Tayma record, in combination with charged aquifers, had distinct short-term impacts on the local environment and probably also on human migration. Vegetation resources[4] and the abundance of prey animals[12] increased and stimulated Neolithic migrations into Northern Arabia as indicated by abundant Levant-type Pre-Pottery Neolithic A and B assemblages identified in the Northern branch of the Nefud desert[10,11].

## Methods

**Tayma sediment cores**. Drilling on today's sabkha of the Tayma palaeolake basin was performed in 2011 and 2013 using an Atlas Copco vibracoring device (Cobra mk1) fitted with closed steel auger heads and PVC liners with a diameter of 5 cm. Two series of ca. 6 m long sediment cores (Tay 220/221 and Tay 253/254/255/256) capturing the entire Holocene sequence and reaching down to Ordovician sandstone (Qasim Formation) were obtained in close vicinity ('mastercores' in Supplementary Fig. 1a). They each consist of two parallel, overlapping core sequences A and B with 1 m-long core sections. The cores were opened and photographically documented at the University of Cologne (Laboratory for Physical Geography) and GFZ Potsdam, Germany. The construction of composite profiles and correlation of the sediment cores is based on 24 macroscopic lithological marker layers (fixed marker horizons, FMH). Archive cores of the master site are stored and accessible in the core storage facility of the Institute of Geography, Heidelberg University, refrigerated at 4 °C.

Tayma sediment cores were analysed for their sedimentology (XRF [X-ray fluorescence] core scanning, quantitative XRF on discrete samples, semi-quantitative X-ray diffraction, micro-facies analyses on thin sections), geochemistry (elemental analyses, stable isotopes, lipid biomarkers), palynology (vegetation reconstruction through pollen analysis) and micropalaeontology (assemblages of foraminifera, ostracods and diatoms). Here, we used stable isotopes of oxygen and carbon measured on aragonite laminae of the annually laminated (varved) core section ($\delta^{18}O_{arag}$, $\delta^{13}C_{arag}$) as well as bulk carbonates from the entire core ($\delta^{18}O_{carb}$, $\delta^{13}C_{carb}$) in combination with micro-facies analyses of the varved sediments to trace the evolution of the early to mid-Holocene palaeolake at Tayma. Further proxy data have partially been published[4,36,54] or will be presented in forthcoming publications.

In Supplementary Fig. 6, the lithological profile of the ca. 6.5 m-long composite core, TOC content[54], $\delta^{18}O_{carb}$ and $\delta^{13}C_{carb}$ (see Methodological details further down), and statistical clustering results of the XRF core-scanning record are shown. The elemental composition of the sediment core was determined by non-destructive XRF core scanning on the split-core sediment surface using an ITRAX elemental scanner at GFZ Potsdam. Measurements were obtained every 0.2 mm using a Cr X-ray source, operated at 30 kV, 30 mA and 10 s, to capture intensities of the elements Si, S, Cl, K, Ca, Ti, Fe, Sr and Zr. A centred log-ratio (clr = ln [element intensity/geometric mean of all nine elements]) transform was performed for all elements of each measurement to eliminate the influences of physical properties, sample geometry and matrix effects[55,56] and to enable robust statistical analyses[57]. Statistical clustering (Ward's method) of XRF core-scanning results indicates four main sediment groups (Supplementary Fig. 6): Cluster 1 (light grey) is dominated by Si, Ti and Fe and describes the siliciclastic sediments and occurs predominantly in the upper part of the Tayma profile (VII—sabkha phase). Cluster 2 (green) does not show a clear preference, but is rather a mixture of all considered elements, describing clastic, carbonate and evaporitic 'background' sediments. Cluster 3 (blue) is dominated by Sr and Ca and describes aragonite, which occurs exclusively in the varved sediments of the Tayma core representing the deep-lake phases III and IV (Fig. 2e). Cluster 4 (orange) is dominated by the elements S and Ca and mainly describes gypsum that was deposited during the terminal lake phase (V) and thereafter, when wetlands occupied the Tayma basin (phase VI).

TOC indicates the production and preservation of organic matter in the lake and was measured on in situ decalcified samples using an elemental analyser (NC2500 Carlo Erba) at GFZ Potsdam, Germany. Ca. 3 mg of freeze-dried and powdered sample material was weighed into Ag-capsules, treated with 20% HCl, heated and dried for 3 h at 75 °C. The calibration of the data was carried out applying element standards (Acetanilide, Urea). It was verified using a soil reference sample (Boden3, HEKATECH). The reproducibility for replicate samples was ~0.2%[54]. The sediments deposited in the Tayma basin are mainly composed of clay, silt and sand, evaporites (sulphates), authigenic carbonates and in parts high amounts of diatoms (at the mastercore site in the centre of the basin), gastropod shells, ostracods and foraminifera (along the margins of the basin representing the palaeo-shoreline) (Supplementary Fig. 6). Clay- and silt-sized detritus is dominant in the core and was deposited as dark grey, mm- to cm-thick, occasionally graded layers. Coarser silt- to sand-sized minerals (mainly quartz) are scattered in the sediments or are concentrated in the uppermost part of the Tayma profile. Evaporites were mainly identified in the form of whitish-beige, finer-grained laminae of gypsum and other sulphates. Carbonates are present in the form of white, sub-mm thick primary aragonite laminae, and, in the upper part, Mg–carbonate layers. Biogenic carbonates (ostracods, foraminifera, and barnacle and gastropod shell fragments) are dominant along the shorelines of the palaeolake. Their concentration is much lower in the centre of the basin where the mastercore was taken.

**Varve micro-facies analysis**. We used changes in varve micro-facies, i.e. the composition of seasonal sublayers of the annual laminations, to infer changing seasonality and the interannual variability of lake-internal evaporation and productivity. The thickness and composition of varve sublayers were analysed under the microscope along with varve counting on petrographic thin sections. A total of eleven different sublayer types were grouped into five main sediment components (carbonate, organic, clastic, diatoms and gypsum). Data are given as relative contribution (in %) to the varve thickness (Fig. 2e). Raw data of micro-facies sublayer thicknesses are presented in Supplementary Fig. 9.

**Age model construction**. Due to the absence of datable terrestrial macroscopic plant remains in Tayma cores and reported hard-water effects altering radiocarbon ages from gastropods, ostracods and *Ruppia* seeds for up to 1500 years[4,15], preliminary age models[4,54] were based on AMS radiocarbon dating of pollen grains, as these are unsusceptible to incorporating old carbon[58,59]. Pollen extraction from a total of 33 samples of 1–13 cm long sediment sections followed a combination of physical and chemical separation protocols[58–61]. Sample preparation included sieving (at 6, 20, 40 and 70 µm), treatment with heated HCl, KOH and $H_2SO_4$, and heavy-liquid density separation using CsCl and sodium polytungstate.

Varve counting was performed on 14 large-scale (10 cm × 1.5 cm) petrographic thin sections using a Leica DMLP petrographic microscope under semi-/fully polarised light and with 50× magnification. Thin sections were prepared following standard procedures for soft sediments[62] including freeze-drying and impregnation with epoxy resin (Araldite 2020). Sawing and polishing were performed manually under dry conditions to avoid salt crystallisation. Multiple counting and the definition of correlation marker layers ensured a negligible subjective counting error. Counting uncertainty due to poor sublayer quality is ±40 varves (6.2%).

The age-depth model was constructed with Bacon v2.2 using flexible Bayesian modelling[63] including implemented outlier analysis and the IntCal13 atmospheric calibration curve[64]. All 38 radiocarbon ages of pollen concentrate, other plant remains (*Ruppia* seeds, non-pollen palynomorphs, charred plant particles), two mollusc samples, as well as a tephrochronological anchor identified close to the base of the Tayma sediment record (the central Anatolian 'S1' tephra dated at 8983 ± 83 cal yr BP in the Dead Sea)[35], were considered for age modelling (Supplementary Data 1). The floating varve chronology of 650 ± 40 varve years served to refine the Bayesian model within the varved section. The start of varve formation is defined by $^{14}$C dating to 8549 cal yr BP (8470–8605 cal yr BP for the 95.4% probability range). Based on this fixed point (F1), the varve age of a turbidite layer at 8138 ± 40 varve years BP and the end of varve formation at 7900 ± 40 varve years BP were used as further fix points (F2 and F3) in the adjusted Bayesian model (Supplementary Fig. 7).

Outlier analysis reliably discarded samples ($n = 6$) containing ≤50% pollen or hard-water-affected material (gastropod shells, *Ruppia* seeds), and 13 samples with ≥50% pollen unsuitable for the Bayesian age-depth model. All remaining 18 $^{14}$C ages of pollen concentrate included in the final model contained high pollen concentrations of at least 50% (Supplementary Data 1, Supplementary Fig. 7).

**Reconstruction of hydroclimatic conditions**. The stable isotope composition of lake water ($\delta^{18}O_{water}$ and $\delta D_{water}$) in closed lakes is mainly controlled by precipitation and evaporation and reflects hydrological changes and moisture sources[43]. The $\delta^{18}O_{carb}$ ($\delta^{13}C_{carb}$) values of bulk carbonates and $\delta D_{nC29,\ nC31}$ from fossil leaf waxes in lake sediments are proxies for hydroclimatic conditions and were used to reconstruct the precipitation, lake-water evaporation and temperature during the early to mid-Holocene. To assess the hydrological balance of the Tayma palaeolake (8800–7950 cal yr BP), the wetland (7800–6800 cal yr BP), and the potential moisture sources during the HHP, we compared calculated $\delta D_p$ (precipitation) and $\delta^{18}O_{water}$ (lake water) values with the isotopic characterisation of the main regional atmospheric systems, recent precipitation, as well as surface and groundwater isotope compositions (Supplementary Fig. 8).

**Stable oxygen and carbon isotopes**. Stable oxygen and carbon isotope measurements ($\delta^{13}C_{carb}$ and $\delta^{18}O_{carb}$) were performed on the carbonate fraction of a total of 262 freeze-dried and ground samples taken in cm slices from core Tay 220. Bulk samples of ~0.4 mg were loaded into 10 ml Labco Exetainer vials automatically flushed with He and reacted in phosphoric acid (100%) at 75 °C for 60 min[65]. The stable isotope compositions were determined at GFZ Potsdam using a Finnigan GasBenchII with carbonate option coupled to a DELTAplusXL IRMS (isotope ratio mass spectrometer) (Thermo Fisher Scientific). For finer resolution and to exclude biogenic carbonates, we sampled pure primary aragonite of laminae from dried and impregnated sediment blocks by drilling. The aragonite samples of about 0.06 mg were measured for $\delta^{18}O_{arag}$ and $\delta^{13}C_{arag}$ at GFZ Potsdam with an automated carbonate device (KIEL IV) coupled to a Finnigan MAT253 IRMS (Thermo Fisher Scientific) on cryogenically purified $CO_2$ released by dissolution with 103% $H_3PO_4$ at 72 °C for 10 min. Oxygen and carbon isotope compositions are given relative to the VPDB (Vienna Peedee Belemnite) standard in conventional delta notation $\delta$ (‰). Calibration was performed using international reference standards (NBS18 and NBS19). For both methods, standard deviations ($1\sigma$) for reference and replicate analyses are better than 0.08‰ for both $\delta^{18}O$ and $\delta^{13}C$.

In closed lakes, $\delta^{18}O_{carb}$ values mainly reflect hydrological changes and are used as a proxy for precipitation, groundwater influx and lake evaporation because: (i) seasonality and temperature have little effect on oxygen isotope fractionation of precipitation in low-latitude regions[43,66]; (ii) the lake-water oxygen isotopic composition in an endorheic basin is governed by evaporation under arid climate conditions resulting in increased $\delta^{18}O_{water}$; (iii) equilibrium oxygen isotope fractionation is assumed for inorganic carbonates; and (iv) primary inorganic carbonates precipitate during the spring–summer season induced by evaporation and/or phytoplankton bloom in the epilimnion. The latter is consistent with increasing $\delta^{13}C_{carb}$ values, indicating $^{12}$C depletion of the total dissolved inorganic carbon due to atmospheric release and/or preferential use of aquatic plants.

The calculation of $\delta^{18}O_{VSMOW}$ palaeolake water from $\delta^{18}O_{VPDB}$ values using the re-expressed relationship of ref. [67] in the simplified Eq. (1) according to ref. [43]

$$T = 13.8 - 4.58(\delta c - \delta w) \quad (1)$$

under equilibrium water ($w$)-calcite ($c$) precipitation at a temperature ($T$ in °C) of 21 °C (as the average temperature in spring) and an offset of +0.6‰ for aragonite and magnesium bearing calcite reveals comparable $\delta^{18}O$ values between precipitated carbonates and hot water. The modelled mean $\delta^{18}O_{water}$ for the palaeolake water is high with +8.4‰ and, thus, much lighter due to freshwater inflow of surface and groundwater than for the wetland with a calculated mean $\delta^{18}O_{water}$ of +13.1‰ due to lower precipitation and high evaporation.

**Stable hydrogen isotopes of leaf-wax *n*-alkanes ($\delta D_{wax}$)**. Stable hydrogen isotopes of leaf-wax n-alkanes ($\delta D_{wax}$) were measured on 64 samples from core Tay 255. Samples were taken in 1 cm-slices, freeze-dried and ground for lipid biomarkers extraction at the Max Planck Institute for Biogeochemistry in Jena. 5–15 g of the sample was extracted using a 40 ml dichloromethane:methanol (9:1) mixture at 100 °C and 120 bar for 15 min in two consecutive cycles using a BÜCHI SpeedExtractor. The total lipid extract was separated into aliphatic, aromatic and alcohol/fatty acid fractions using solid-phase extraction on silica gel according to the method presented in ref. [68]. The aliphatic hydrocarbon fraction was desulfurized using HCl-activated copper (15% HCl). Identification and quantification of *n*-alkanes were accomplished using a GC-MS (Agilent Technologies, 7890A GC-System; 220 Ion trap MS) by comparing peak areas and retention times with an external *n*-alkane standard mixture (*n*C16 to *n*C36). Compound-specific hydrogen isotope ratios (expressed as δD) of the *n*-alkanes were measured on a DELTA V$^{Plus}$ IRMS (Thermo Fisher Scientific) coupled to an Agilent 7890 GC (Agilent Technologies) at GFZ Potsdam. Every sample was measured in triplicates. The mean standard deviation of all measured samples was 3‰. The δD values were normalised to the Vienna Standard Mean Ocean Water (VSMOW).

The changes in $\delta D_{wax}$ of the lake records are interpreted as indicators for the variability in precipitation, humidity and vegetation type[66,68,69]. Hydrogen isotopes $\delta D_{nC29,\ nC31}$ of terrestrial leaf wax $nC_{29}$ and $nC_{31}$ *n*-alkanes were used to calculate $\delta D_p$ between precipitation ($p$) according to refs. [38,39,69]. The negative isotopic fractionation from $\delta D_p$ to $\delta D_{wax}$ due to the incorporation of hydrogen in leaf waxes has been calculated using Eq. (2)

$$\delta D_p = [(\delta D_{wax} + 1000)/((\varepsilon/1000) + 1)] - 1000 \quad (2)$$

with $\varepsilon = -130$ for $nC_{29}$ and $nC_{31}$ *n*-alkanes representing the mixture of C3/C4 plant waxes of grasses, shrubs and trees that can be expected for the region[4] (Supplementary Fig. 8). Following ref. [5], we inferred the precipitation rate from $\delta D_p$ values. The relationship of precipitation and rainfall amount for the Sahara region described a non-linear dependence with a steep slope in $\delta D_p$ values below 100 mm yr$^{-1}$ and a strong influence of the amount effect.

**$\delta^{18}O_{water}$ and $\delta D_{water}$ isotopes of water samples**. Filtered water samples of groundwater from the historical Bir Haddaj well of the Tayma oasis, from the Tay 255 borehole in the palaeolake, and evaporated rainwaters from small water pools south of the palaeolake taken shortly after a rain event in December 2015, were triple-measured at the GFZ for $\delta^{18}O_{water}$ and $\delta D_{water}$ relative to VSMOW using Cavity Ring-Down spectrometers (PICARRO L2120-i and L2130-i). Analytical precision of VSMOW and SLAP calibrated analyses was <1‰ for both $\delta^{18}O_{water}$ and $\delta D_{water}$.

The isotopic fractionation of lake-water evaporation was calculated for the remaining lake water sampled in December 2015 ($\delta^{18}O_{rw}$) using initial groundwater-supported lake water with $\delta^{18}O_{iw}$ of −3‰ with simple Rayleigh distillation after Eq. (3)

$$\delta^{18}O_{rw} = \delta^{18}O_{iw} - 1000(f^{(\alpha-1)} - 1) \quad (3)$$

where $\alpha$ = fractionation factor between water and vapour at 21 °C[70] and $f$ = fraction of remaining lake water.

**Reconstruction of palaeo-moisture source and lake-water evaporation**. The few meteoric water samples from Tabuk (IAEA) plot with $\delta^{18}O_p$ ~−1‰ closely to the global meteoric water line (GMWL), except for one lighter sample tending more to the Eastern Mediterranean meteoric water line (EMMWL). Recent (12/2015) evaporated rainwater samples collected in water pools in a wadi SW of the Tayma palaeolake show slightly enriched $\delta^{18}O_{water}$ and $\delta D_{water}$ values of around −0.5‰. Using $\delta D_{wax}$ to estimate past precipitation rates as explained above reveals the lowest values of about −2‰ $\delta D_p$ for the wetland phase and values as low as −28‰ for the palaeolake (Supplementary Fig. 8), indicating higher rainfall amounts between 8800 and 7950 cal yr BP due to increased precipitation and a probable amount effect.

The stable isotopes of the historical Bir Haddaj well in Tayma, one of the largest and most prominent historical wells on the Arabian Peninsula[71,72] that taps the uppermost level of the Saq aquifer, reflect subsurface groundwater with −3.5‰ $\delta^{18}O_{water}$ and −24.6‰ $\delta D_{water}$, similar to the middle of the Saq aquifer further south[73,74]. The water from the palaeolake sampled in 1.5 m depth of the well Tay 255 in 2015 with +7.4‰ $\delta^{18}O_{water}$ and +16.2‰ $\delta D_{water}$ probably reflects porewater isotope composition. The portion of surface-water evaporation calculated using Rayleigh fractionation between −3‰ $\delta^{18}O_{water}$ for groundwater and +7.4‰ $\delta^{18}O_{water}$ for the Tay 255 well reaches about 70% for the deep lake phase and >80% for the wetland phase. The isotopic difference between the deep palaeolake and the wetland water is mainly influenced by decreases in precipitation and increasing evaporation.

Although the three main atmospheric systems affecting the northwestern Arabian Peninsula (Indian Monsoon, Mediterranean Westerlies and African Monsoon) show isotopic fingerprints with more or less variation and deuterium excess, it is unreasonable to decipher the moisture sources during the time of palaeolake formation due to the determination of precipitation $\delta D_p$ using $\delta D_{wax}$ and $\delta^{18}O_{carb}$ being indirect, as well as associated fractionation effects. In general, the moisture source-related isotope fingerprints over the Arabian Peninsula are masked by strong evaporation, continental and altitude effects, sub-cloud evaporation, moisture recycling and the amount effect[75].

## Data availability

Data reported here are stored at GFZ Data Services (https://doi.org/10.5880/GFZ.4.3.2021.005) and freely accessible under a Creative Commons Attribution 4.0 International License (CC BY 4.0)[76]. Further supplementary data and information are available as Supplementary Material and Supplementary Data in the online version of the paper. Correspondence and requests for materials should be addressed to M.E.

## Code availability

This study does not use custom code or mathematical algorithm that is deemed central to the conclusions.

Received: 21 June 2021; Accepted: 28 January 2022;
Published online: 04 March 2022

## References

1. Jennings, R. P. et al. The greening of Arabia: multiple opportunities for human occupation of the Arabian Peninsula during the Late Pleistocene inferred from an ensemble of climate model simulations. *Quat. Int.* **382**, 181–199 (2015).
2. Parton, A. et al. Alluvial fan records from southeast Arabia reveal multiple windows for human dispersal. *Geology* **43**, 295–298 (2015).
3. Breeze, P. S. et al. Palaeohydrological corridors for hominin dispersals in the Middle East ~250–70,000 years ago. *Quat. Sci. Rev.* **144**, 155–185 (2016).
4. Dinies, M., Plessen, B., Neef, R. & Kürschner, H. When the dessert was green: grassland expansion during the early Holocene in northwestern Arabia. *Quat. Int.* **382**, 293–302 (2015).
5. Tierney, J. E., Pausata, F. S. R. & deMenocal, P. B. Rainfall regimes of the Green Sahara. *Sci. Adv.* **3**, e1601503 (2017).
6. Nicholson, S. L., Hosfield, R., Groucutt, H. S., Pike, A. W. & Fleitmann, D. Beyond arrows on a map: the dynamics of *Homo sapiens* dispersal and occupation of Arabia during Marine Isotope Stage 5. *J. Anthropol. Archaeol.* **62**, 101269 (2021).
7. Armitage, S. J. et al. The southern route "Out of Africa": evidence for an early expansion of modern humans into Arabia. *Science* **331**, 453–456 (2011).
8. Groucutt, H. S. et al. *Homo sapiens* in Arabia by 85,000 years ago. *Nature Ecol. Evol.* **2**, 800–809 (2018).
9. Crassard, R., Hilbert, Y. H., Preusser, F., Wulf, G. & Schiettecatte, J. Middle Palaeolithic occupations in central Saudi Arabia during MIS 5 and MIS 7: new insights on the origins of the peopling of Arabia. *Archaeol. Anthropol. Sci.* **11**, 3101–3120 (2019).
10. Crassard, R. et al. Beyond the Levant: First evidence of a Pre-Pottery Neolithic incursion into the Nefud Desert, Saudi Arabia. *PLoS ONE* **8**, e68061 (2013).
11. Petraglia, M. D., Groucutt, H. S., Guagnin, M., Breeze, P. S. & Boivin, N. Human responses to climate and ecosystem change in ancient Arabia. *Proc. Natl Acad. Sci. USA* **117**, 8263–8270 (2020).
12. Guagnin, M. et al. Rock art imagery as a proxy for Holocene environmental change: a view from Shuwaymis, NW Saudi Arabia. *Holocene* **26**, 1822–1834 (2016).
13. Arz, H. W., Lamy, F., Pätzold, J., Müller, P. J. & Prins, M. Mediterranean moisture source for an Early-Holocene Humid Period in the northern Red Sea. *Science* **300**, 118–121 (2013).
14. Enzel, Y., Kushnir, Y. & Quade, J. The middle Holocene climatic records from Arabia: reassessing lacustrine environments, shift of ITCZ in Arabian Sea, and impacts of the southwest Indian and African monsoons. *Glob. Planet. Change* **129**, 69–91 (2015).
15. Engel, M. et al. Lakes or wetlands? A comment on 'The middle Holocene climatic records from Arabia: Reassessing lacustrine environments, shift of ITCZ in Arabian Sea, and impacts of the southwest Indian and African monsoons' by Enzel et al. *Glob. Planet. Change* **148**, 258–267 (2017).
16. Kutzbach, J. E. & Liu, Z. Response of the African Monsoon to orbital forcing and ocean feedbacks in the middle Holocene. *Science* **278**, 440–443 (1997).
17. Rosenberg, T. M. et al. Middle and Late Pleistocene humid periods recorded in palaeolake deposits of the Nafud desert, Saudi Arabia. *Quat. Sci. Rev.* **70**, 109–123 (2013).
18. Shanahan, T. M. et al. The time-transgressive termination of the African Humid Period. *Nat. Geosci.* **8**, 140–144 (2015).
19. Kutzbach, J. E., Chen, G., Cheng, H., Edwards, R. L. & Liu, Z. Potential role of winter rainfall in explaining increased moisture in the Mediterranean and Middle East during periods of maximum orbitally-forced insolation seasonality. *Clim. Dyn.* **42**, 1079–1095 (2014).
20. Rubin, S., Ziv, B. & Paldor, N. Tropical plumes over eastern North Africa as a source of rain in the Middle East. *Mon. Weather Rev.* **135**, 4135–4148 (2007).
21. Tubi, A., Dayan, U. & Lensky, I. M. Moisture transport by tropical plumes over the Middle East: a 30-year climatology. *Q. J. R. Meteorol. Soc.* **143**, 3165–3176 (2017).
22. Waldmann, N., Torfstein, A. & Stein, M. Northward intrusions of low- and mid-latitude storms across the Saharo-Arabian belt during past interglacials. *Geology* **38**, 567–570 (2010).
23. Skinner, C. B. & Poulsen, C. J. The role of fall season tropical plumes in enhancing Saharan rainfall during the African Humid Period. *Geophys. Res. Lett.* **43**, 349–358 (2016).
24. Hausleiter, A., Eichmann, R. & Al-Najem, M. (eds.). *Taymā' I* (Archaeopress, Oxford, 2018).
25. Breeze, P. S. et al. Remote sensing and GIS techniques for reconstructing Arabian palaeohydrology and identifying archaeological sites. *Quat. Int.* **382**, 98–119 (2015).
26. Bar-Matthews, M., Ayalon, A., Gilmour, M., Matthews, A. & Hawkesworth, C. J. Sea–land oxygen isotopic relationships from planktonic foraminifera and speleothems in the Eastern Mediterranean region and their implication for paleorainfall during interglacial intervals. *Geochim. Cosmochim. Acta* **67**, 3181–3199 (2003).
27. Grant, K. M. et al. Rapid coupling between ice volume and polar temperature over the past 150,000 years. *Nature* **491**, 744–747 (2012).
28. Cheng, H. et al. The climate variability in northern Levant over the past 20,000 years. *Geophys. Res. Lett.* **42**, 8641–8650 (2015).
29. Fleitmann, D. et al. Holocene ITCZ and Indian monsoon dynamics recorded in stalagmites from Oman and Yemen (Socotra). *Quat. Sci. Rev.* **26**, 170–188 (2007).
30. Cheng, H. et al. Timing and structure of the 8.2 kyr B.P. event inferred from $\delta^{18}O$ records of stalagmites from China, Oman, and Brazil. *Geology* **37**, 1007–1010 (2009).
31. Schulz, E. & Whitney, J. W. Upper Pleistocene and Holocene lakes in the An Nafud, Saudi Arabia. *Hydrobiologia* **143**, 175–190 (1986).
32. Parton, A. et al. Middle-late Quaternary palaeoclimate variability from lake and wetland deposits in the Nefud Desert, Northern Arabia. *Quat. Sci. Rev.* **202**, 78–97 (2018).
33. Zielhofer, C. et al. Climate forcing and shifts in water management on the Northwest Arabian Peninsula (mid-Holocene Rasif wetlands, Saudi Arabia). *Quat. Int.* **473**, 120–140 (2018).
34. Engel, M. et al. The early Holocene humid period in NW Saudi Arabia—sediments, microfossils and palaeo-hydrological modelling. *Quat. Int.* **266**, 131–141 (2012).
35. Neugebauer, I. et al. Implications of S1 tephra findings in Dead Sea and Tayma palaeolake sediments for marine reservoir age estimation and palaeoclimate synchronisation. *Quat. Sci. Rev.* **170**, 269–275 (2017).
36. Pint, A. et al. How to discriminate athalassic and marginal marine microfaunas: Foraminifera and other fossils from an early Holocene continental lake in northern Saudi Arabia. *J. Foram. Res.* **47**, 175–187 (2017).
37. Parker, A. et al. A record of Holocene climate change from lake geochemical analyses in southeastern Arabia. *Quat. Res.* **66**, 465–476 (2006).
38. Sachse, D. et al. Molecular paleohydrology: interpreting the hydrogen-isotopic composition of lipid biomarkers from photosynthesizing organisms. *Annu. Rev. Earth Planet. Sci.* **40**, 221–249 (2012).
39. Collins, J. A. et al. Estimating the hydrogen isotopic composition of past precipitation using leaf-waxes from western Africa. *Quat. Sci. Rev.* **65**, 88–101 (2013).
40. Ginau, A., Engel, M. & Brückner, H. Holocene chemical precipitates in the continental sabkha of Tayma (NW Saudi Arabia). *J. Arid Environ.* **84**, 26–37 (2012).
41. Garber, R., Levy, Y. & Friedman, G. The sedimentology of the Dead Sea. *Carbonates Evaporites* **2**, 43–57 (1987).
42. Heim, C., Nowaczyk, N., Negendank, J., Leroy, S. & Ben-Avraham, Z. Near East desertification: evidence from the Dead Sea. *Naturwissenschaften* **84**, 398–401 (1997).
43. Leng, M. J. & Marshall, J. D. Palaeoclimate interpretation of stable isotope data from lake sediment archives. *Quat. Sci. Rev.* **23**, 811–831 (2004).
44. Ben Dor, Y. et al. The paleohydrological implications of aragonite precipitation under contrasting climates in the endorheic Dead Sea and its precursors revealed by experimental investigations. *Chem. Geol.* **576**, 120261 (2021).
45. Torfstein, A., Gavrieli, I., Katz, A., Kolodny, Y. & Stein, M. Gypsum as a monitor of the paleo-limnological–hydrological conditions in Lake Lisan and the Dead Sea. *Geochim. Cosmochim. Acta* **72**, 2491–2509 (2008).
46. Arz, H. W., Lamy, F. & Pätzold, J. A pronounced dry event recorded around 4.2 ka in brine sediments from the northern Red Sea. *Quat. Res.* **66**, 432–441 (2006).
47. IAEA & WMO. Global Network of Isotopes in Precipitation. *The GNIP Database*. https://nucleus.iaea.org/wiser (2018).
48. Rohling, E. J. & Palike, H. Centennial-scale climate cooling with a sudden cold event around 8,200 years ago. *Nature* **434**, 975–979 (2005).
49. Gasse, F. Hydrological changes in the African tropics since the Last Glacial Maximum. *Quat. Sci. Rev.* **19**, 189–211 (2000).
50. Blanchet, C. L. et al. High- and low-latitude forcing of the Nile River regime during the Holocene inferred from laminated sediments of the Nile deep-sea fan. *Earth Planet. Sci. Lett.* **364**, 98–110 (2013).

51. Rohling, E. J., Marino, G. & Grant, K. M. Mediterranean climate and oceanography, and the periodic development of anoxic events (sapropels). *Earth Sci. Rev.* **143**, 62–97 (2015).
52. Tesi, T. et al. Large-scale response of the Eastern Mediterranean thermohaline circulation to African monsoon intensification during sapropel S1 formation. *Quat. Sci. Rev.* **159**, 139–154 (2017).
53. Pross, J. et al. Massive perturbation in terrestrial ecosystems of the Eastern Mediterranean region associated with the 8.2 kyr BP climatic event. *Geology* **37**, 887–890 (2009).
54. Dinies, M., Neef, R., Plessen, B. & Kürschner, H. In *The Archaeology of North Arabia: Oases and Landscapes* (ed. Luciani, M.) 57–78 (Austrian Academy of Sciences Press, 2016).
55. Weltje, G. J. & Tjallingii, R. Calibration of XRF core scanners for quantitative geochemical logging of sediment cores: theory and application. *Earth Planet. Sci. Lett.* **274**, 423–438 (2008).
56. Weltje, G. J. et al. In *Micro-XRF Studies of Sediment Cores* (eds Croudace, I. W. & Rothwell R. G.) 507–534 (Springer, Dordrecht, 2015).
57. Aitchison, J. The statistical analysis of compositional data. *J. R. Stat. Soc. Ser. B* **44**, 139–160 (1982).
58. Brown, T. A., Nelson, D. E., Mathewes, R. W., Vogel, J. S. & Southon, J. R. Radiocarbon dating of pollen by accelerator mass spectrometry. *Quat. Res.* **32**, 205–212 (1989).
59. Vandergoes, M. J. & Prior, C. A. AMS Dating of pollen concentrates—a methodological study of late Quaternary sediments from South Westland, New Zealand. *Radiocarbon* **45**, 479–491 (2003).
60. Regnéll, J. & Everitt, E. Preparative centrifugation—a new method for preparing pollen concentrates suitable for radiocarbon dating by AMS. *Veg. Hist. Archaeobot.* **5**, 201–205 (1996).
61. Nakagawa, T. et al. Dense-media separation as a more efficient pollen extraction method for use with organic sediment/deposit samples: comparison with the conventional method. *Boreas* **27**, 15–24 (1998).
62. Brauer, A. & Casanova, J. Chronology and depositional processes of the laminated sediment record from Lac d'Annecy, French Alps. *J. Paleolimnol.* **25**, 163–177 (2001).
63. Blaauw, M. & Christen, J. A. Flexible paleoclimate age-depth models using an autoregressive gamma process. *Bayesian Anal.* **6**, 457–474 (2011).
64. Reimer, P. J. et al. IntCal13 and Marine13 radiocarbon age calibration curves 0–50,000 Years cal BP. *Radiocarbon* **55**, 1869–1887 (2013).
65. Spötl, C. & Vennemann, T. W. Continuous-flow isotope ratio mass spectrometric analysis of carbonate minerals. *Rapid Commun. Mass Spectrom.* **17**, 1004–1006 (2003).
66. Bowen, G. J. Isoscapes: spatial pattern in isotopic biogeochemistry. *Annu. Rev. Earth Planet. Sci.* **38**, 161–187 (2010).
67. Kim, S.-T. & O'Neil, J. R. Equilibrium and nonequilibrium oxygen isotope effects in synthetic carbonates. *Geochim. Cosmochim. Acta* **61**, 3461–3475 (1997).
68. Sachse, D., Radke, J. & Gleixner, G. δD values of individual n-alkanes from terrestrial plants along a climatic gradient—implications for the sedimentary biomarker record. *Org. Geochem.* **37**, 469–483 (2006).
69. Aichner, B. et al. Hydroclimate in the Pamirs was driven by changes in precipitation-evaporation seasonality since the last glacial period. *Geophys. Res. Lett.* **46**, 13972–13983 (2019).
70. Horita, J. & Wesolowski, D. J. Liquid-vapor fractionation of oxygen and hydrogen isotopes of water from the freezing to the critical temperature. *Geochim. Cosmochim. Acta* **58**, 3425–3437 (1994).
71. Hausleiter, A. In *Cultural heritages of water—the cultural heritages of water in the Middle East and Maghreb* (ed. ICOMOS) 313–343 (UNESCO World Heritage Convention, International Council on Monuments and Sites, 2017).
72. Wellbrock, K. et al. In *Taymā' I* (eds. Hausleiter, A., Eichmann, R. & al-Najem, M.) 145–198 (Archaeopress, Oxford, 2018)
73. Al-Sagaby, A. & Moallim, A. Isotopes based assessment of groundwater renewal and related anthropogenic effects in water scarce areas: sand dunes study in Qasim area. *Saudi Arabia. IAEA-TECDOC* **1246**, 221–229 (2001).
74. Alyamani, M. S. Isotopic composition of rainfall and ground-water recharge in the western province of Saudi Arabia. *J. Arid Environ.* **49**, 751–760 (2001).
75. Michelsen, N. et al. Isotopic and chemical composition of precipitation in Riyadh, Saudi Arabia. *Chem. Geol.* **413**, 51–62 (2015).
76. Neugebauer, I. et al. Geochemical and sedimentological data of the Tayma palaeolake record. *GFZ Data Services*. https://doi.org/10.5880/GFZ.4.3.2021.005.
77. Fick, S. E. & Hijmans, R. J. WorldClim 2: new 1-km spatial resolution climate surfaces for global land areas. *Int. J. Climatol.* **37**, 4302–4315 (2017).
78. Akçar, N. & Schlüchter, C. Paleoglaciations in Anatolia: a schematic review and first results. *E&G Quat. Sci. J.* **55**, 102–121 (2005).
79. Wellbrock, K., Strauss, M., Külls, C. & Grottker, M. In *Des refuges aux oasis: Vivre en milieu aride de la Préhistoire à aujourd'hui. XXXVIIIe rencontres internationales d'archéologie et d'histoire d'Antibes* (eds. Purdue, L., Charbonnier, J. & Khalidi, L.) 231–249 (Éditions APDCA, 2018).
80. Danielson, J. J. & Gesch, D. B. Global multi-resolution terrain elevation data 2010 (GMTED2010). *USGS Open-File Rep.* 2011–1073 (2011).
81. Laskar, J. et al. A long-term numerical solution for the insolation quantities of the Earth. *Astron. Astrophys.* **428**, 261–285 (2004).
82. Thomas, E. R. et al. The 8.2 ka event from Greenland ice cores. *Quat. Sci. Rev.* **26**, 70–81 (2007).


## Acknowledgements

This study is a contribution to the interdisciplinary research project "CLEAR—Holocene CLimatic Events of Northern ARabia" (https://clear2018.wordpress.com/), funded by Deutsche Forschungsgemeinschaft (DFG grants EN977/2-1, PL535/2-1, FR1489/5-1). The CLEAR project was kindly invited and supported by the Saudi-German Joint Archaeological Project at Tayma, led by Ricardo Eichmann, Arnulf Hausleiter (German Archaeological Institute) and Mohammed H. al-Najem (Museum of Archaeology and Ethnography, Tayma). We are grateful for the research permit issued by the Saudi Commission for Tourism and National Heritage, represented by HRH Prince Sultan bin Salman bin Abdulaziz al-Sa'ud. Permissions to export core samples were kindly granted under the umbrella of the Joint Saudi-German Archaeological Project at Tayma. Further support by Jenny Friedrich (sample preparation), Sylvia Pinkerneil (GFZ) (hydrogen isotope measurements on water), Doreen Noack, Andrea Vieth-Hillebrand (GFZ) (hydrogen isotope measurements on n-alkanes), Dieter Berger (GFZ) (preparation of thin sections), Christin Kramer (documentation) and Kirstin Jacobson (language editing) is greatly appreciated. Detailed comments of three anonymous reviewers greatly improved the paper. For the publication fee we acknowledge financial support by Deutsche Forschungsgemeinschaft within the funding programme "Open Access Publikationskosten" as well as by Heidelberg University and GFZ Potsdam.

## Author contributions

B.P., I.N., M.E. and P.F. designed the study. M.E., H.B., M.D. and A.P. collected the sediment cores. M.D. and I.N. constructed the age model. I.N., B.P., R.T., P.H. and A.B. contributed the sedimentological and microfacies data. B.P and I.N. contributed stable-isotope data on water and carbonates. N.D., V.F.S. and G.G. contributed the leaf-wax n-alkane data. A.P. and P.F. contributed foraminiferal and ostracod analyses. A.S. and K.J.K. contributed the diatom analysis. I.N., M.E. and B.P. wrote the paper. All authors discussed and commented on the paper.

## Competing interests

The authors declare no competing interests.

## Additional information

**Supplementary information** The online version contains supplementary material available at https://doi.org/10.1038/s43247-022-00368-y.

**Correspondence** and requests for materials should be addressed to Max Engel.

**Peer review information** *Communications Earth & Environment* thanks Jonathan Dean and the other, anonymous, reviewer(s) for their contribution to the peer review of this work. Primary Handling Editor: Joe Aslin. Peer reviewer reports are available.

**Reprints and permission information** is available at http://www.nature.com/reprints

**Publisher's note** Springer Nature remains neutral with regard to jurisdictional claims in published maps and institutional affiliations.